Material Model Fidelity Comparison for the Efficacy of Predicting Residual Stresses in L-PBF Additively Manufactured IN718 Components

David P. Failla, Jr. [1,2,3], Matthew J. Dantin [4], Chuyen J. Nguyen [3,5] and Matthew W. Priddy [1,3,*]

[1] Michael W. Hall School of Mechanical Engineering, Mississippi State University, Mississippi State, MS 39762, USA; dpf39@msstate.edu
[2] U.S. Army Engineer Research and Development Center, Vicksburg, MS 39180, USA
[3] Center for Advanced Vehicular Systems, Mississippi State University, Mississippi State, MS 39759, USA
[4] Naval Surface Warfare Center Carderock Division, West Bethesda, MD 20817, USA
[5] Department of Computer Science & Engineering, Mississippi State University, Mississippi State, MS 39762, USA
[*] Correspondence: mwpriddy@me.msstate.edu

Abstract: Internal state variable models are well suited to predict the effects of an evolving microstructure as a result of metal-based additive manufacturing (MBAM) processes in components with complex features. As advanced manufacturing techniques such as MBAM become increasingly employed, accurate methods for predicting residual stresses are critical for insight into component performance. To this end, the evolving microstructural model of inelasticity (EMMI) is suited to modeling these residual stresses due to its ability to capture the evolution of rate- and temperature-dependent material hardening as a result of the rapid thermal cycling present in MBAM processes. The current effort contrasts the efficacy of using EMMI with an elastic–perfectly plastic (EPP) material model to predict the residual stresses for an Inconel 718 component produced via laser powder bed fusion (L-PBF). Both constitutive models are used within a thermo-mechanical finite element framework and are validated by published neutron diffraction measurements to demonstrate the need for higher-fidelity models to predict residual stresses in complex components. Both EPP and EMMI can qualitatively predict the residual stresses trends induced by the L-PBF local raster scanning effects on the component, but the influence of the temperature-dependent yield and lack of plastic strain hardening allowed EPP to perform similar to EMMI away from free surfaces. EMMI offered the most insight at the free surfaces and around critical component features, but this work also highlights EMMI as a process–property-dependent model that needs be calibrated to specimens produced with a similar reference structure for microstructure evolution effects to be accurately predicted.

Keywords: additive manufacturing; thermomechanical modeling; internal state variable models; residual stress; finite element method; inconel alloys

1. Introduction

Metal-based additive manufacturing (MBAM) is an advanced manufacturing process by which a component is fabricated through adding metal material to build a component, rather than by removing or casting material [1,2]. MBAM commonly consists of depositing material in a layer-by-layer fashion that is then fused together through melting the deposited material with a moving heat source. This methodology is executed with a variety of different mechanisms, including laser powder bed fusion (L-PBF) [3], directed energy deposition (DED) [1], and wire-arc additive manufacturing (WAAM) [4]. The process of melting and solidifying between each layer occurs rapidly, which induces residual stresses that can impact component performance in terms of fatigue life [5] and can cause part cracking [6] and part deformation [4,7,8]. For example, as the initial layer is deposited,

it solidifies and achieves mechanical equilibrium via expansion. After the next layer is deposited and subsequently melted, the surface between the two layers begins to interact. As the current layer material is melted, heat is conducted through it to the previous layers, causing them to expand. However, the previously deposited layer and current layer heat to different temperatures, and therefore have different cooling rates. This mismatch in cooling rates causes the parts to shrink non-uniformly, which induces a combined tension and compression state in the component. These effects are further exacerbated by the addition of more layers and subsequent thermal cycling. These residual stresses are strongly influenced by the machine process parameters used [9–12]. The machine process parameters include, but are not limited to, laser power, laser scan speed, layer thickness, and scan strategy [13]. Therefore, designers must perform numerous experiments to determine optimal machine process parameter sets for a given material for each MBAM technique. To aid in this endeavor, numerical methods have been developed to model MBAM processing effects on fabricated components. Amongst the most common methods employed for part-scale models are finite element (FE) sequentially coupled thermomechanical simulations that model the response of the part during fabrication [14–17]. For L-PBF, the FE method can be employed by using a moving heat source to represent the laser combined with an element birth and death technique [18,19] through a progressive element activation scheme to mimic the powder deposition for each layer [7]. This allows for the nodal temperature histories to be used as initial conditions to solve for the thermally induced stresses in the mechanical model. For material response, a number of modeling efforts employ an elastic-perfectly plastic (EPP) material model [14] with temperature-dependent properties [20], while others attempt to account for the inherent anisotropy induced as an artifact of the MBAM process or stress relaxation in the form of a relaxation temperature [21]. A higher fidelity material modeling approach can be accomplished through leveraging internal state variable (ISV) models, which attempts to predict the effects of the lower-length scales on the continuum scale. However, little research has been done to predict the thermomechanical effects of the MBAM process with ISV models outside of an implementation of a modified Bammann–Chiesa–Johnson (BCJ) material model [22] and the Evolving Microstructural Model of Inelasticity (EMMI) for DED modeling [23].

The cyclic temperature history observed during the L-PBF process results in a continually changing microstructure. The resultant microstructure and its associated features such as dislocation movement, phase transformation, and hardening, directly contribute to the as-built component's residual stresses, distortion, and mechanical properties. Thus, accounting for the evolutionary history of a component's features with a physically based ISV modeling methodology will better connect the machine process parameters with the component's mechanical response compared to modeling approaches that do not account for the microstructural effects of processing history. The proposed ISV model of interest in this work is EMMI. Although EMMI was primarily developed to capture the effects of high strain rate finite deformation of metals [24], the large fluctuations in temperature and thermal cycling along with resultant distortion and residual stresses make EMMI an ideal candidate to model the process due to its temperature dependence and ability to capture the evolution of hardening. While this work focuses on L-PBF, EMMI has been used to model DED in previous work with success [23]. The primary features of EMMI used in this work are as follows: (i) the elastic modulus is temperature- and damage-dependent; (ii) plasticity is described by isotropic and kinematic hardening variables and models both the hardening and recovery mechanisms that characterize the dislocations and cell structures formed during deformation.

The constitutive models employed in this work are temperature-dependent EPP and EMMI to represent low- and high-fidelity modeling approaches, respectively. The implementation of EMMI in this work evaluates whether more physically informed material models are needed for more accurate residual stress predictions. The aim for this effort is to contrast predictions for the residual stresses experienced in an L-PBF produced part of Inconel 718 (IN718) with complex geometry features such as fillets and holes by contrasting

with neutron diffraction results [25] for validation to further develop an understanding of material modeling fidelity limitations and needs for MBAM.

2. Materials and Methods

All simulations leveraged Abaqus/Standard 2019 [26]. The thermal simulation was conducted on a local machine using a 32-core AMD Threadripper. The thermal results were then transferred to a Cray CS300-LC cluster, where 3 nodes with 20 threads per node were used to solve for the mechanical response. No graphical processing unit (GPU) acceleration was used for these simulations [27]. Both the EPP and EMMI implementations used the same thermal history input for the FE sequentially coupled thermomechanical framework to predict the mechanical response for an accurate comparison [28]. The computer aided designs (CAD) were developed using Solid Edge 2023 [29], and meshing was accomplished using Coreform Cubit 2022.6 [30].

2.1. L-Shape Geometry

To contrast the efficacy of EMMI with an EPP model, a component with complex features such as curved edges and holes was needed. The adopted geometry as shown in Figure 1 is replicated from [25], where neutron diffraction was performed on the beamline KOWARI with the Australian Nuclear Science and Technology Organization (ANSTO) to determine internal residual stresses on the L-PBF produced component. To mimic the L-PBF post-processing, the part was extruded an additional 0.4 mm down to capture the stress relief and material loss in the part from wire electrical discharge machine (EDM) removal. The part was modeled on square substrate with a depth of 12.7 mm. The entire substrate was not modeled to reduce computational costs, and the size was reduced to a square cross-sectional area of 65 mm × 65 mm to allow for there to be at least 10 mm all around the component. Both the substrate and the L-shape part were assumed to be fully dense, and any porosity was assumed to be negligible. The substrate is not shown in Figure 1 for clarity. The modeled materials for the component and substrate were IN718 and 316 L, respectively. The cross-sections labeled C2 and C3 intersecting the hole shown in Figure 1 will be of focus for characterizing residual stresses around complex geometries.
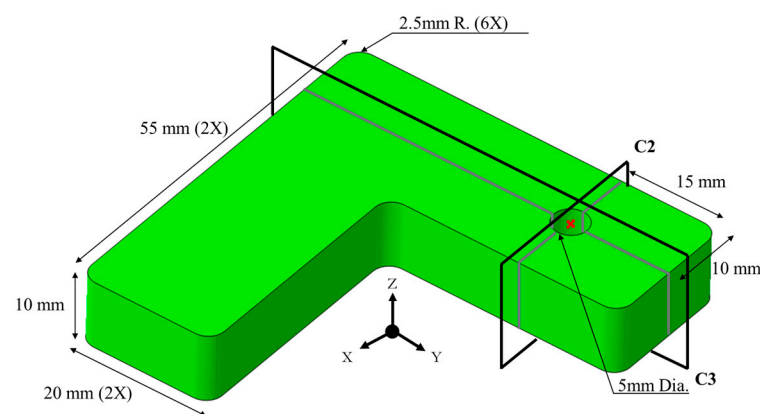

Figure 1. Image of L-shape part showing the C2 and C3 cross–sections intersecting the hole of interest to compare with experimental measurements.

2.2. Mesh

Partitions were made to the geometry along the cross-sections C2 and C3, as shown in Figure 1, to ensure nodes and element faces were on the cross-sections to match experimental measurement locations without interpolating. An additional partition was added between the part and the substrate for sectional property assignments. A non-uniform mesh with a static adaptive mesh refinement was leveraged for element mesh generation [31], where the element size increased through the powder and substrate to reduce computational cost but maintain accuracy for the component. The thermal mesh

formulated consisted of the part on the substrate surrounded by powder, as illustrated in Figure 2a, with a total of 688,636 DC3D8 elements. For the mechanical analysis, the element type was changed to C3D8R, and the elements associated with powder were removed since the powder will have a negligible contribution to the mechanical response of the part [32]. The edges of the part were seeded at 0.4 mm, whereas the rest of the part had a global seed size of 2.5 mm using a sweep meshing scheme. The seed size of 0.4 mm was used to allow for 25 element layers to be progressively activated to represent the L-PBF process. The mesh consisted of a single part, and therefore, tie constraints between the substrate, part, and powder were not needed. Furthermore, this approach uses a lumped-mass assumption, as each element layer represents 10 layers of powder to reduce computational costs [15]. Mesh quality was determined through the aspect ratio as illustrated in Figure 2b.
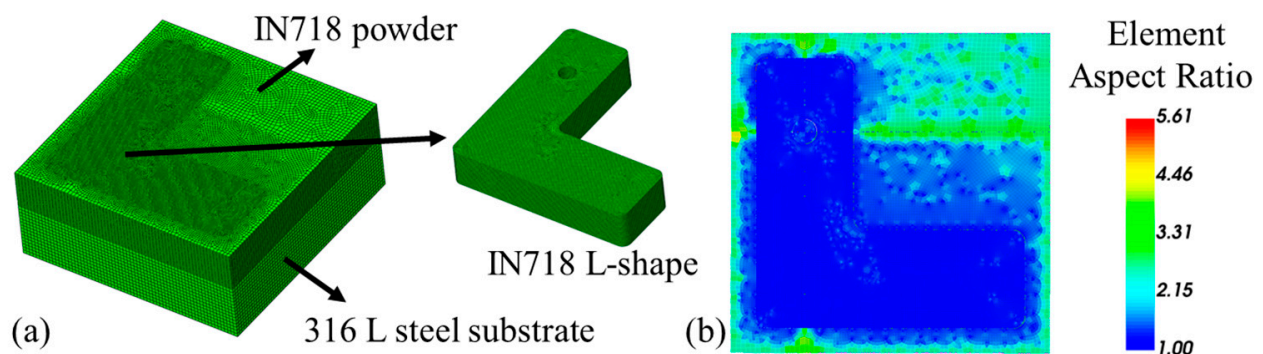

Figure 2. (**a**) The mesh used for the thermal model was partitioned into three sections for applying different materials models to each: the part, the powder, and the substrate. The elements associated with the powder were removed for mechanical analysis. (**b**) Mesh element aspect ratio contour to illustrate quality of mesh from the top-down view. Element density was coarsened in the powder and substrate since they were not the area of interest, but were still needed to capture their effects on the part.

The average aspect ratio for the L-shape part was 1.04, while the average aspect ratio was allowed to change and deviate more for the powder and substrate, as shown in Table 1.

Table 1. Mesh quality metrics.

Aspect Ratio	L-Shape	Powder	Substrate
Average	1.04	1.64	2.29
Minimum	1.00	1.00	1.00
Maximum	1.66	4.52	5.61

2.3. Loads and Boundary Conditions

For the thermal model, an initial and two heat-transfer simulation steps were defined for the printing and cooling processes. As outlined in Table 2, the substrate was assigned an initial temperature to mimic the heated chamber, while the elements associated with the deposited material were initialized to room temperature upon activation. The deposited material represents both the L-shape part and the un-melted powder, as illustrated in Figure 2a.

For the mechanical model, the bottom surface nodes of the substrate were fixed and the elements associated with the powder were removed to reduce computational time. As each layer of elements was activated in the mechanical model, a relaxation temperature of 750 °C [33] was assigned to all elements, and then each element was prescribed a set of nodal temperatures as determined from the output of thermal analysis. Following the cooling step in the mechanical model, a cut removal step via *MODEL CHANGE in Abaqus was leveraged to remove the elements that made up the additional 0.4 mm of thickness

added to separate the part from the substrate. Separate steps were used to mimic actual post-processing conditions. The mechanical output at the end of each step is shown in Figure 3.

Table 2. Thermal loading steps and boundary conditions.

| Thermal Loading and Boundary Conditions			
Step	Description	316L steel substrate	IN718 L-Shape and Powder
1	Initialization	Substrate initialized to 200 °C	Deposited material progressively initialized to 23 °C
2	Material Deposition/Printing	Nodes on substrate bottom surface fixed to 200 °C	Constant convection and radiation applied to exterior surfaces with sink temperature of 200 °C
			Concentrated moving heat source dictated by event series applied to L-shape part
3	Cooling	Nodes on substrate bottom surface fixed to 23 °C	Constant convection and radiation applied to exterior surfaces with sink temperature of 23 °C
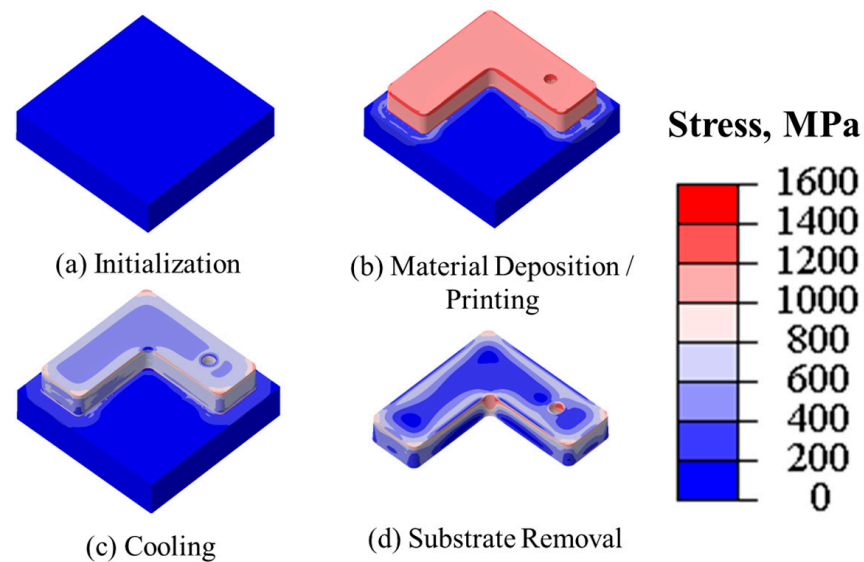
Figure 3. The mechanical simulation showing von Mises stresses consists of 4 steps: (**a**) initialization of substrate and initial boundary conditions, (**b**) predictions of stresses as a result of the layer-wise printing, (**c**) stress relaxation predictions from cooling, (**d**) predictions of stress as part achieves equilibrium after being removed from the substrate.

Automatic incrementation was used to determine the stable time increment [26] with the maximum for the thermal and mechanical models set to 20 s and 50 s, respectively, during printing. The minimum stable time increment was set to 1×10^{-5} s for both the thermal and mechanical modes. In addition, the thermal simulation used an output time series based on the generated event series to force Abaqus to adjust the increment size to solve for the temperatures at key event times during the printing process [34]. These key event times were defined as before element layer activation, immediately before raster scanning, at 5 interval time points during the raster scanning, and at the end of raster scanning. The output cycle was repeated for all layers during the thermal model and was used to provide the key points of the thermal history to the mechanical model. This significantly reduced the computational time of using a specified increment size and allowed for a larger time increment to be used.

2.4. Thermal Modeling

The governing equation for the transient heat conduction that drives and dominates the thermal model is portrayed in Equation (1):

$$\rho C_p \frac{\partial T}{\partial t} = \nabla \cdot (-\kappa \nabla T) + Q \tag{1}$$

where ρ is the material density; C_p is the specific heat capacity; T is the temperature; t is the time; κ is the thermal conductivity; and Q represents the thermal load from the heat source. The thermal load consists of the heat contributions from the conduction via the concentrated moving heat source, convection, and radiation. The convection heat transfer is determined using Newton's law of cooling as illustrated in Equation (2):

$$q_{conv} = h(T_S - T_\infty) \tag{2}$$

where h is the convection heat transfer coefficient; T_S is the surface temperature of the part; and T_∞ is the sink temperature. The convection heat transfer coefficient for the whole model was assumed constant at 15 W/m^{2}K from [5]. The radiation effects are accounted for with the Stefan–Boltzmann law as shown in Equation (3):

$$q_{rad} = \sigma \varepsilon \left(T_S^4 - T_\infty^4 \right) \tag{3}$$

where ε is the emissivity and σ is the Stefan–Boltzmann constant. The emissivity for the whole model was assumed constant at 0.3 from [5]. A concentrated moving heat source is used to represent the conduction from the laser. This strategy was implemented over other models such as a Goldak Ellipsoidal model [35] due to the elements being much larger than the laser spot size and for computational efficiency [36]. This assumption is reasonable due to the high speed of the laser with respect to the size of the elements and the overall size of the part, and the cross-section in the build-direction has minimal variance throughout the build [10]. The laser process parameters for laser power and speed were 200 W and 900 mm/s for the infill and a 100 W and 450 mm/s for the contour, respectively, to reflect the build from [25]. The scan strategy, or heat source path, via the event series selected was meander. The original component was printed using a stripe scan strategy, but due to event series generation limits, meander was used. The difference in the effects of these scan strategies for this component are then assumed to be negligible. The CAD file used for mesh generation was also used to develop a g-code file via Slic3r [37] as shown in Figure 4.
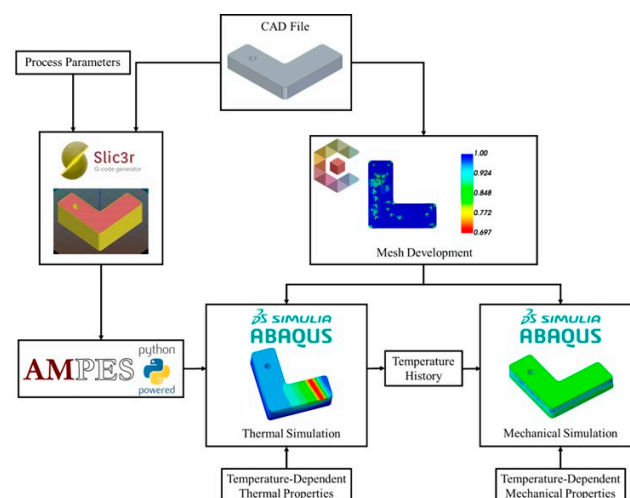

Figure 4. Thermomechanical modeling flow showing transition from CAD to mesh and process parameters and from CAD to g-code to the AMPES-generated event series to create inputs for the thermal and mechanical models.

The machine process parameters derived from [25] alongside the g-code files generated by Slic3r were provided as inputs to AMPES [34], a Python event series generation preprocessing tool that uses a RepRap flavored g-code file to create print-path event series for use with numerical solvers. The resulting input power and theoretical volumetric energy density, as estimated from the generated event series are shown in Figure 5a and Figure 5b, respectively. The input volumetric energy density was approximated using Equation (4) from [13].

$$ED_{est} = \frac{P\left(\frac{1}{hatch \cdot v}\right)}{t} \tag{4}$$

where ED_{est} is the estimated input volumetric energy density; P is the input power; *hatch* is the hatch spacing; v is the laser speed; and t is the layer thickness. The meshed files designed in Cubit paired with the generated event series were used as the input to Abaqus to implicitly simulate the thermal and mechanical response of the component. See Appendices A and C for thermal material constants for IN718 and 316L, respectively. Approximating an interlayer dwell time [38] of 180 s with 347 layers, the total step time for printing was computed by AMPES to be 73,249 s, or 20.3 h, which is assumed to be close to how long the L-shape parts from [25] took to fabricate with the selected L-PBF machine process parameters.
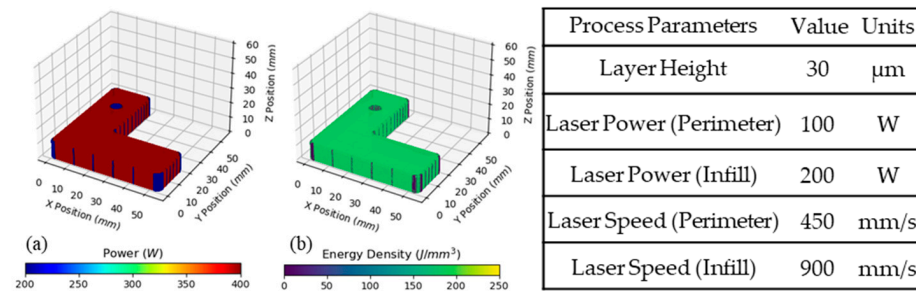

Process Parameters	Value	Units
Layer Height	30	μm
Laser Power (Perimeter)	100	W
Laser Power (Infill)	200	W
Laser Speed (Perimeter)	450	mm/s
Laser Speed (Infill)	900	mm/s

Figure 5. (**a**) Power and (**b**) theoretical input volumetric energy density plotted in 3D space as estimated by the generated event series with associated machine process parameters from [25].

2.5. Mechanical Modeling—Elastic–Perfectly Plastic

The EPP model assumes that no hardening occurs in the material system shown in Equation (5):

$$\varepsilon = \begin{cases} \frac{\sigma}{E} & \sigma < \sigma_y \\ \varepsilon_{el} + \varepsilon_{pl} + \varepsilon_{th} & \sigma \geq \sigma_y \end{cases} \tag{5}$$

where ε is the total strain; ε_{el} is the elastic strain contribution; ε_{pl} is the plastic strain contribution; ε_{th} is the thermal strain contribution; σ is the nominal stress; σ_y is the yield stress of the material; and E is the Young's Modulus. Though the actuality of a material foregoing any form of strain hardening or thermal softening is unrealistic, the amount of hardening can be small enough in ductile metals for the use of the EPP model as an approximation. For the purposes of demonstrating the robustness of EMMI to capture flow stress, the limitations of EPP serve to stress the need for a physically based ISV. The mechanical strains are interpreted from the prescribed nodal temperatures via thermal expansion given as:

$$\varepsilon^{th} = \alpha\left(T, f_\beta\right)\left(T - T^0\right) - \alpha\left(T^I, f_\beta^I\right)\left(T^I - T^0\right) \tag{6}$$

where α thermal expansion coefficient; f_β are the current values for the predefined field variables; T^0 is the reference temperature; T^I is the initial temperature; f_β^I are the initial value of the of the field variables [26]. These strains are related to stress via Hooke's law:

$$\sigma = C\varepsilon \tag{7}$$

where C is a rank four material stiffness tensor. Mechanical properties for IN718 and 316L are listed in Appendices B and D, respectively.

2.6. Mechanical Modeling—Evolving Microstructural Model of Inelasticity

EMMI was developed to predict the inelastic response of metals in environments containing high strain rate and large fluctuations in temperature. Thus, EMMI is an ideal candidate to model the L-PBF process due to the aforementioned rapid thermal cycling observed. EMMI is a dislocation mechanics-based ISV model and is the successor to the widely used BCJ plasticity model [39]. Relevant updates to EMMI from BCJ include updated equations representing changes to strain rate effects and recovery mechanisms. These updates position EMMI as more physically based than BCJ, particularly in the formulation of plasticity. Furthermore, as an ISV model, EMMI captures state variables to track the cyclic temperature history, hardening, and recovery effects observed in the L-PBF process. The version of EMMI used in this work was modified to include the relaxation of deviatoric stresses, hardening variables, and plastic strains above 80% of the melting temperature of the metal [23]. The assumption that justifies this modification lies in the physical basis of increased dislocation motion that occurs above 80% of the melting temperature resulting in annihilation of work hardening which is caused by the metal behaving as a linear viscous material [40]. Furthermore, the implemented version of EMMI was based upon three features: (i) the temperature dependence of yield strength and Young's Modulus; (ii) isotropic and kinematic hardening variables to track the evolution of plasticity; and (iii) hardening and recovery mechanisms that represent the cell structures and dislocations created under deformation.

The finite strain deformation gradient, F, is multiplicatively decomposed into the following: (i) the thermal deformation gradient, F_θ, (ii) the deviatoric plastic deformation gradient, F_p, (iii) the volumetric deformation gradient, F_d, and (iv) the elastic recoverable deformation gradient, F_e [24]. Thus, the total deformation gradient is shown in Equation (8). Damage is neglected in this implementation due to the relatively small strain nature of L-PBF.

$$F = F_e F_d F_p F_\theta \tag{8}$$

The plastic strain is represented by three equations: (i) the inelastic flow rule, (ii) isotropic hardening, and (iii) kinematic hardening. The inelastic flow rule is shown in Equation (9), where $\overline{\sigma}_{eq}$ is the equivalent stress, $\overline{\kappa_s}$ is internal stress due to isotropic hardening, $Y(\theta)$ is the temperature-dependent yield function, and $f(\theta)$ is a temperature-dependent material parameter. The strain rate due to isotropic hardening, $\dot{\overline{\varepsilon}}_s$, is shown in Equation (10), where H is a hardening material constant, $R_D(\theta)$ is a dynamic recovery constant, and $R_s(\theta)$ and $Q_s(\theta)$ are temperature-dependent static recovery constants. The strain rate due to kinematic hardening, $\dot{\overline{\beta}}$, is shown in Equation (11), where h is a hardening material constant, $r_d(\theta)$ is a temperature-dependent dynamic recovery constant, and $\overline{\beta}$ is isotropic hardening. The calibration constants used in this study can be found at reference [41]. Further documentation for EMMI can be found in Marin et al. [24]. See Appendix E for EMMI material parameters used.

$$\dot{\overline{\varepsilon}}^p = f(\theta)\left[sinh\left(\langle\frac{\overline{\sigma}_{eq}}{\overline{\kappa_s} + Y(\theta)} - 1\rangle\right)\right]^n \tag{9}$$

$$\dot{\overline{\varepsilon}}_s = [H - R_D(\theta)\overline{\varepsilon}_s]\dot{\overline{\varepsilon}}^p - R_s(\theta)\overline{\varepsilon}_s sinh[Q_s(\theta)\overline{\varepsilon}_s] \tag{10}$$

$$\dot{\overline{\beta}} = hF^{eT}d^p F^e - r_d(\theta)\dot{\overline{\varepsilon}}\sqrt{\frac{2}{3}}\|\overline{\beta}\|\overline{\beta} \tag{11}$$

3. Results

The computational resources used for the thermal model and mechanical models with each material model are listed in Table 3. The total runtime for all jobs was about

100 h, or just over 4 days. This framework then offers significant computational time savings over using a smaller increment size and no initial temperature in the mechanical model. Through preliminary runs using a fixed time increment size of 0.4 s with similar mass lumping assumptions, the thermal model was estimated to have taken 3 to 4 months to finish, which was not feasible. This also did not account for the mechanical model predictions, which usually take much longer on account of the added degrees of freedom. It is also important to note that the thermal model took longer to solve due to its much smaller time increment scheme, as noted in Section 2.3. This resulted in the thermal model having 3191 increments, as opposed to the EPP and EMMI mechanical model predictions having 498 and 504 increments, respectively. Despite having fewer degrees of freedom, the smaller increment size combined with fewer computing threads resulted in a much higher runtime than the mechanical model predictions. Lastly, the thermal predictions were solved on a different thread count than the mechanical predictions due to resource availability.

Table 3. Computational resources used.

	Thermal	**EPP**	**EMMI**
Thread Count	32	60	60
Element Count	688,636	540,176	540,176
Runtime (h)	62.6	17.2	20

Figure 6 shows the moving heat source at the final increment of the final layer. The expected thermal gradation outlined in the literature is qualitatively present [42], as shown in Figure 6a, and the laser radiation penetration depth is shallow, as expected for IN718 being printed with L-PBF [43], as shown in Figure 6b. The temperatures experienced by the part due to the heat source were approximately 350 °C, and it provided those thermal histories around the hole. This is the rationale for using an initial temperature of 750 °C [33] in the mechanical models as a relaxation temperature [21]. This approach provides more information on the local raster scanning effects on residual stresses at complex features than just layer heating by combining the initialized temperature in the mechanical model with the lower temperatures from the local raster scanning at key time points.
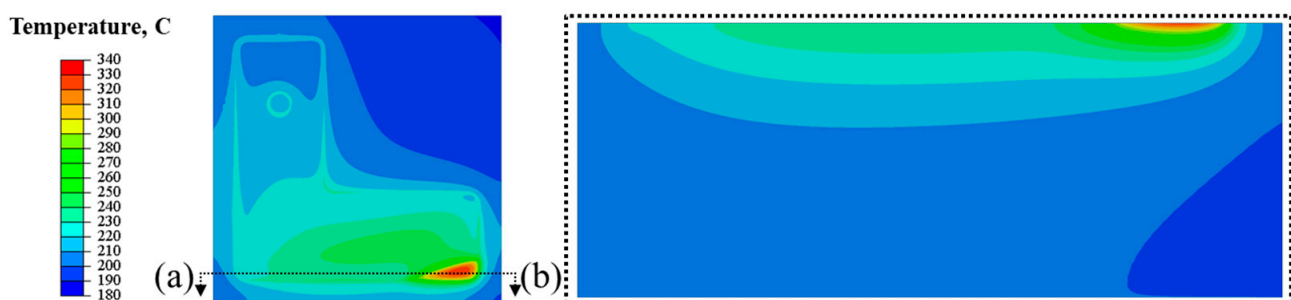

Figure 6. Predicted thermal history dictated by moving heat source at final increment of a layer during printing of (**a**) top view and (**b**) front view cross-section.

3.1. Mechanical Model Results—Surface C2

The mechanical models show the general qualitative trend of AM produced parts, with tensile stress states at the free surfaces and compression internally, as shown in the literature [25,44]. Contrasting EMMI with EPP, EMMI tends to yield much higher residual stresses as opposed to EPP in Figure 7, with the greatest deviation being along the sides of the hole in the build direction.
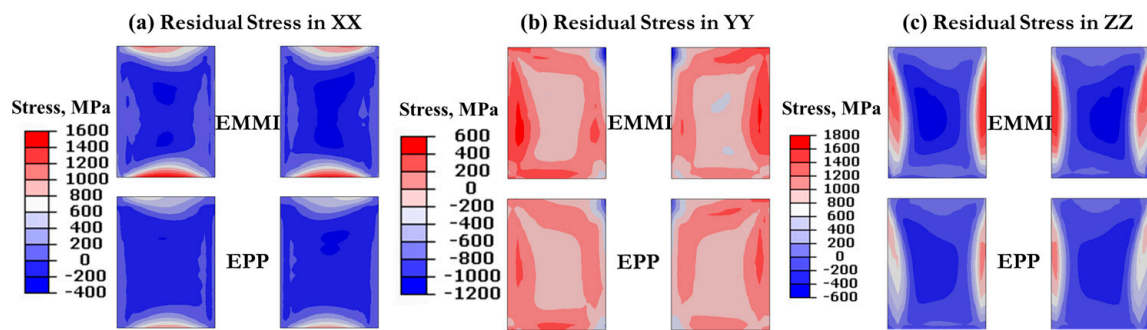
Figure 7. Predicted EPP and EMMI residual stress contours for stresses in (**a**) XX, (**b**) YY, and (**c**) ZZ directions for cross–section C2.

By observing the residual stresses along the line of measurement in Figure 8 on cross-section C2, it is determined that both EPP and EMMI capture the inflection of tensile to compressive to tensile again for all principal stress directions, showing that both models can qualitatively capture the stress response. However, the compressive stresses predicted by both EPP and EMMI are much stiffer than the experimental observation by as much as 200 MPa. Lastly, both models show higher extrema closer to free surfaces, but due to the implementation of the neutron diffraction measurements not approaching the free surface, these simulation points cannot be validated.
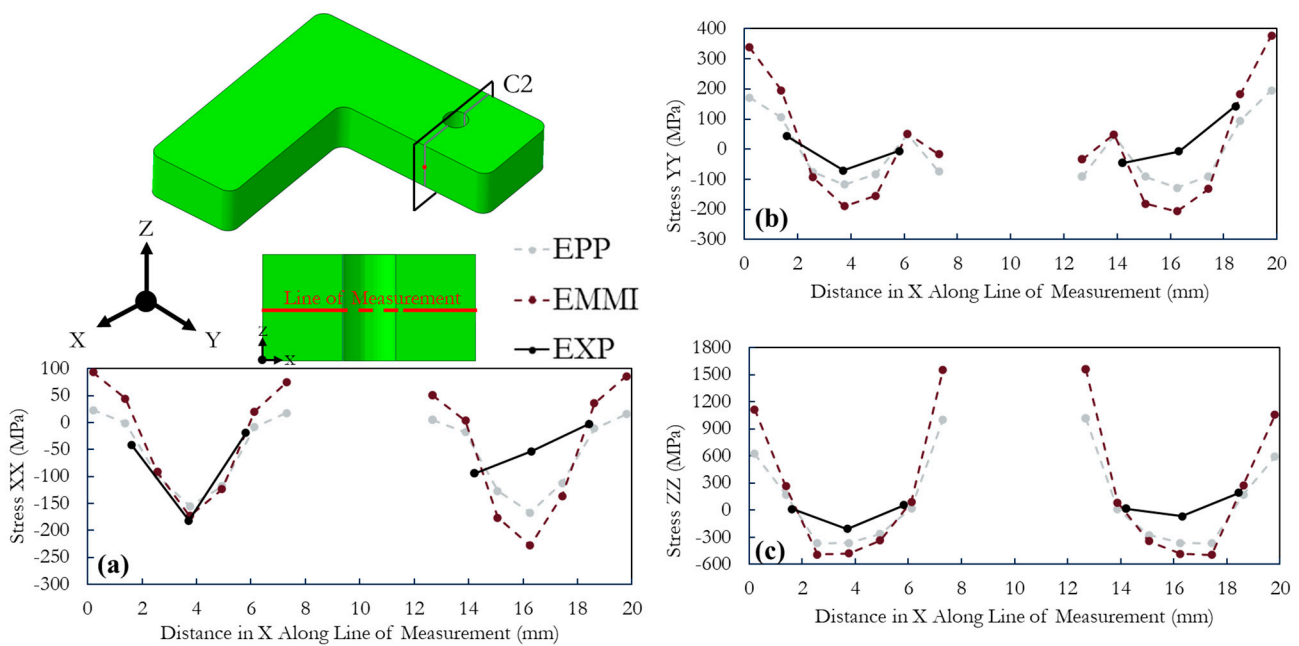

Figure 8. The predicted EPP and EMMI residual stresses (dashed lines) contrasted with the experimentally measured (EXP, solid lines) residual stresses [5] in the (**a**) XX, (**b**) YY, and (**c**) ZZ along the line of measurement on cross–section C2.

3.2. Mechanical Model Results—Surface C3

Similar findings can be found with cross-section C2 for cross-section C3 when contrasting EPP and EMMI in Figures 9–11. The stress extrema predicted by EMMI are higher for both tensile and compressive states, with the stresses in the YY and ZZ at the surface of the hole being the most notable.
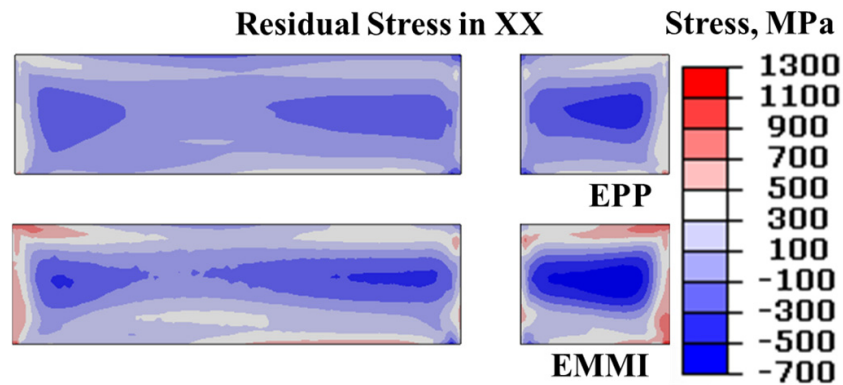
Figure 9. Predicted EPP and EMMI residual stress contours for stress in XX for cross–section C3.
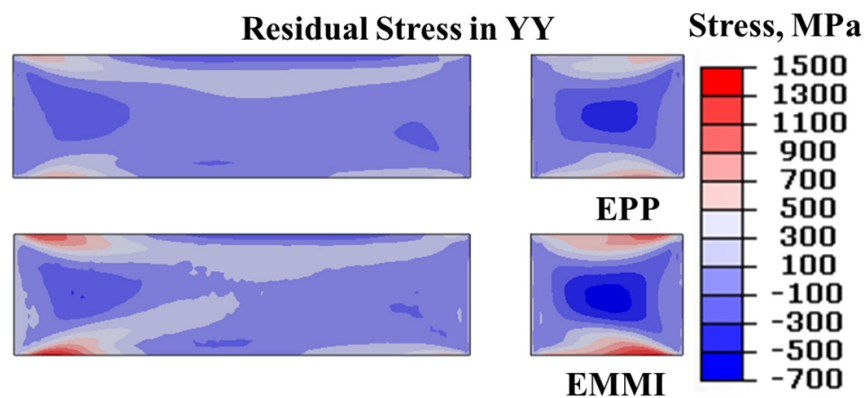

Figure 10. Predicted EPP and EMMI residual stress contours for stress in YY for cross–section C3.
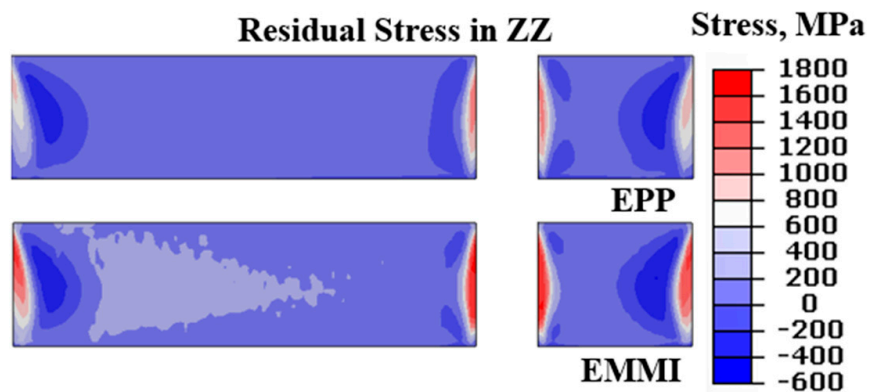

Figure 11. Predicted EPP and EMMI residual stress contours for stress in ZZ for cross–section C3.

Qualitatively, both models yield a similar stress contour to the neutron diffraction results. Interestingly, EPP outperforms EMMI for the stress measurements along the line of measurement from Figure 12 for both the YY and ZZ principal stress directions, highlighting that there is artificial hardening being induced by EMMI for the stress predictions. Furthermore, based on the performance of EPP and the minimal plastic stresses observed, it would show that temperature dependent yield is what drives the residual stresses in the selected L-PBF component produced with the given machine process parameters.
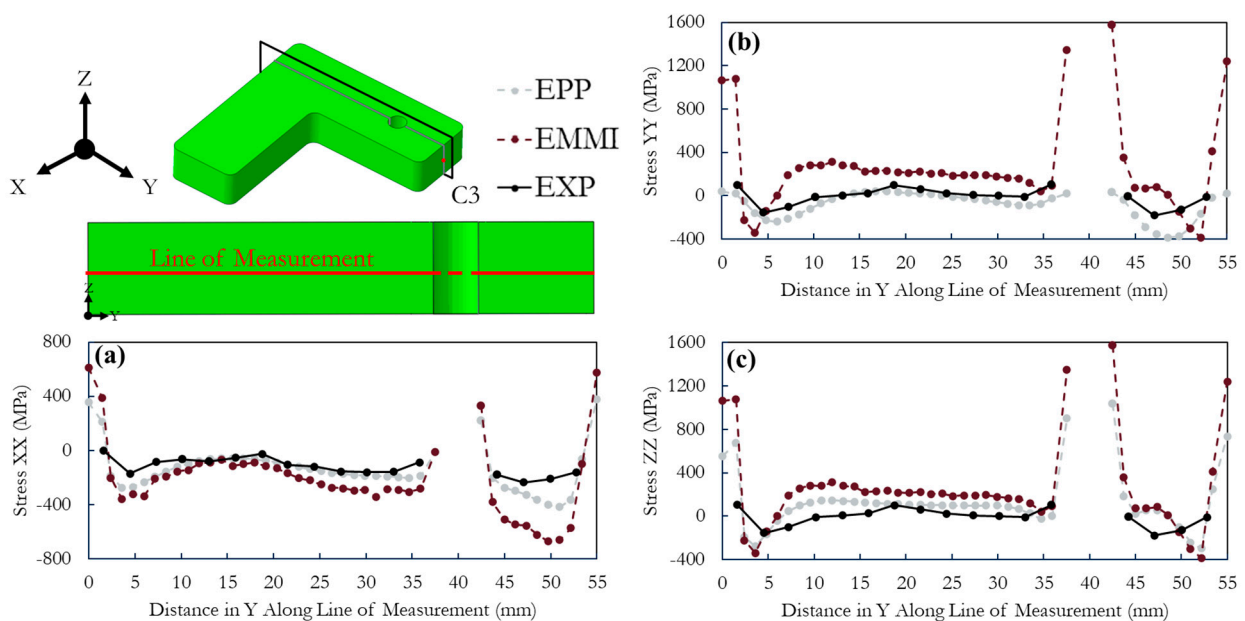
Figure 12. The predicted EPP and EMMI residual stresses (dashed lines) contrasted with the experimentally measured (EXP, solid lines) residual stresses [5] in the (**a**) XX, (**b**) YY, and (**c**) ZZ along the line of measurement on cross–section C3.

3.3. Modeling Limitations

Due to the size of the mesh and nature of the L-PBF simulation process, an h-refinement was not feasible for this effort, and the mesh became dependent on aspect ratio for quality assurance. Furthermore, due to the lack of experimental in-situ thermal history data, quantitative thermal model validation via heat source spot size or thermal gradation through the build height was not possible. Also, due to larger time increments used, the peak temperatures above melt expected from L-PBF are not captured in the thermal predictions and far-field temperatures are used. Lastly, both the L-shape part and substrate were assumed to be fully dense since information on part density was not provided with the neutron diffraction data from [5]. However, from the literature characterizing similar IN718 L-shape parts [45] and determining that porosity was present, it is likely that the referenced L-shape part modeled in this effort also had porosity throughout. By not accounting for this porosity in the current work, stress predictions are likely to over-predict where porosity is dense in the L-shape part due to the inability of the L-shape part to carry a high load in these regions.

4. Conclusions

A comparison between neutron diffraction experimental results and numerical predictions produced through FE methods leveraging EMMI and EPP material models of the induced residual stresses from L-PBF was made. Key takeaways from the comparison are as follows:

- Leveraging lower raster scanning temperatures at key event points with an initialized temperature equivalent to the relaxation of the given material in the mechanical model provides a reasonable amount of far-field thermal history information to predict residual stresses accurately.
- Stresses were the highest at the free surfaces, shown both experimentally and numerically.
- The localized stresses at regions of complex features such as holes demonstrate the need to account for local raster scanning effects in numerical models.
- Plastic hardening appears to have little effect on the L-PBF response away from the free surfaces of the L-shape part, as determined experimentally.

- Both EPP and EMMI qualitatively agree with the neutron diffraction measurements for stress on the C2 and C3 surfaces.
- The residual stresses in the L-shape part are strongly influenced by the temperature-dependent properties of the IN718 material.
- The influence of the temperature-dependent yield on the solution and lack of plastic strain induced hardening in areas away from free surfaces allowed for EPP to more closely match the neutron diffraction measurements than EMMI in some cases, specifically on the cross-section C3 for XX and YY.
- Though not validated by experimental data due to neutron diffraction depth penetration limitations, the stresses at the hole surfaces predicted by EMMI are as much as 67% higher than EPP, which could be attributed to plastic hardening at the free surfaces.
- Both EMMI and EPP struggled to predict maximum compressive stresses in the XX, YY, and ZZ directions on the C3 surface from 45 mm to 52 mm. One explanation for the deviation could be the presence of porosity between the hole and the free surface.

It can be concluded that both EMMI and temperature-dependent EPP material models can provide accurate predictions of residual stresses for complex geometries on the part-scale. However, for both this geometry and material, EPP outperformed EMMI in most cases. One theory for the difference in EPP and EMMI results is attributed to EMMI being calibrated to wrought IN718 [41] as opposed to MBAM-produced IN718 specimens, which have different microstructures. This work therefore highlights the need for future-work where microstructurally sensitive ISV models are calibrated to a reference condition of the selected material system to determine if this could enable EMMI to better predict the effects of the L-PBF process–structure relationship on the desired component. Lastly, the presence of such low experimentally measured maximum stresses from [25] that this study is based on could indicate high amounts of porosity [46,47]. Novel scan strategy work completed for this same L-shape part printed out of IN718 in a different orientation and with different scan strategies [45] further supports this theory. This would also explain why both the EPP and EMMI predictions trended to higher maxima at some locations than the neutron diffraction measurements in Figures 8 and 12, since porosity was assumed to be negligible.

Author Contributions: D.P.F.J.: Writing—review and editing, Writing—original draft, Software, Project administration, Methodology, Investigation, Conceptualization. M.J.D.: Writing—original draft, Writing—review and editing, Investigation, Conceptualization. C.J.N.: Writing—review and editing, Software, Methodology. M.W.P.: Writing—review and editing, Supervision, Project administration, Conceptualization. All authors have read and agreed to the published version of the manuscript.

Data Availability Statement: The original contributions presented in the study are included in the article, further inquiries can be directed to the corresponding author.

Conflicts of Interest: The authors declare that they have no known competing financial interests or personal relationships that could have appeared to influence the work reported in this paper.

Appendix A. IN718 Thermal Material Properties

Temperature-dependent conductivity and specific heat in Table A1 were derived from [5], which were adapted from [48]. Density was taken as 8193 kg/m^3 assumed to be constant and was derived from [49]. The latent heat of fusion of 210 J/g, solidus temperature of 1260 °C, and liquidus temperature of 1336 °C were derived from [50].

Table A1. Temperature-dependent thermal properties of IN718.

Temperature (°C)	Conductivity (W/mK)	Specific Heat (J/kgK)
20	11.4	427
100	12.5	442
300	14	482
500	15.5	522
700	21.5	562
727	21	-
900	-	602
927	25	-
1227	30	-
1350	-	692

Appendix B. IN718 Mechanical Material Properties

Temperature-dependent Young's modulus, yield strength, and coefficient of thermal expansion in Table A2 were derived from [5], which were adapted from [48]. Poisson ratio was taken as 0.3 from [48] and assumed constant.

Table A2. Temperature-dependent mechanical properties of IN718.

Temperature (°C)	Elastic Modulus (GPa)	Yield Strength (MPa)	Coefficient of Thermal Expansion
21	208	1172	-
93	205	1172	1.28×10^{-5}
204	202	-	1.35×10^{-5}
316	194	-	1.39×10^{-5}
427	186	1089	1.42×10^{-5}
538	179	1068	1.44×10^{-5}
649	172	1034	1.51×10^{-5}
760	162	827	1.60×10^{-5}
871	127	286	-
954	17.8	138	-

Appendix C. 316L Thermal Material Properties

Temperature-dependent conductivity and specific heat in Table A3 were derived from [14]. Density was assumed to be constant and taken as 8.0 kg/m^3 from [20]. The latent heat of fusion was taken as 207 J/g [51] and the solidus temperature of 1375 °C and liquidus temperature of 1400 °C were derived from [52].

Table A3. Temperature-dependent thermal properties of 316L.

Temperature (°C)	Conductivity (W/mK)	Specific Heat (J/kgK)
0	12.76	4.40×10^8
159	14.94	5.10×10^8
317	17.18	5.45×10^8
476	19.3	5.60×10^8
634	21.48	5.85×10^8
793	23.66	6.20×10^8
951	25.84	6.50×10^8
1110	28.02	6.80×10^8
1268	30.2	7.13×10^8
1377	-	7.34×10^8
1387	-	6.19×10^9
1417	-	6.19×10^9
1427	32.38	7.44×10^8

Appendix D. 316L Mechanical Material Properties

Temperature-dependent Young's modulus, yield strength, and coefficient of thermal expansion in Table A4 were derived from [14]. Poisson ratio was taken as 0.294 from [20] and assumed constant.

Table A4. Temperature-dependent mechanical properties of 316L.

Temperature (°C)	Elastic Modulus (GPa)	Yield Strength (MPa)	Coefficient of Thermal Expansion
0	200.8	529	1.51×10^{-5}
159	188.9	402.04	1.61×10^{-5}
317	176.3	322.69	1.70×10^{-5}
476	163.1	280.37	1.77×10^{-5}
634	149.1	232.76	1.83×10^{-5}
793	134.6	179.86	1.87×10^{-5}
951	119.3	137.54	1.91×10^{-5}
1110	103.4	89.93	1.92×10^{-5}
1268	86.8	47.61	1.92×10^{-5}
1427	69.5	0.001	1.92×10^{-5}

Appendix E. IN718 EMMI Parameters

The EMMI parameters used were derived from [41] and were used as calibrated. As mentioned before, damage was neglected in this work, and all associated parameters were set to 0. The constants driving the EMMI response in MBAM IN718 are the m_1, m_2, m_3, m_4, and m_5 constants used for the temperature dependent yield function for IN718 from [41] and listed in Table A5.

Table A5. EMMI parameters for temperature-dependent yield function.

Material	m_1	m_2	m_3	m_4	m_5
IN718	1.2321	0.4508	0.14395	11.49	0.67071

References

1. Frazier, W.E. Metal Additive Manufacturing: A Review. *J. Mater. Eng. Perform.* **2014**, *23*, 1917–1928. [CrossRef]
2. Baumers, M.; Dickens, P.; Tuck, C.; Hague, R. The cost of additive manufacturing: Machine productivity, economies of scale and technology-push. *Technol. Forecast. Soc. Chang.* **2016**, *102*, 193–201. [CrossRef]
3. Dunbar, A.J.; Denlinger, E.R.; Gouge, M.F.; Simpson, T.W.; Michaleris, P. Comparisons of laser powder bed fusion additive manufacturing builds through experimental in situ distortion and temperature measurements. *Addit. Manuf.* **2017**, *15*, 57–65. [CrossRef]
4. Wu, B.; Pan, Z.; Ding, D.; Cuiuri, D.; Li, H.; Xu, J.; Norrish, J. A review of the wire arc additive manufacturing of metals: Properties, defects and quality improvement. *J. Manuf. Process.* **2018**, *35*, 127–139. [CrossRef]
5. Pant, P.; Sjöström, S.; Simonsson, K.; Moverare, J.; Proper, S.; Hosseini, S.; Luzin, V.; Peng, R. A Simplified Layer-by-Layer Model for Prediction of Residual Stress Distribution in Additively Manufactured Parts. *Metals* **2021**, *11*, 861. [CrossRef]
6. Holfelder, P.; Brenner, F.; Rund, M.; Witte, A.; Junghans, S.; Seyfert, C.; Richter, M.; Dell, H.; Koukolikova, M.; Gese, H.; et al. Finite element simulation of plasticity and fracture for Inconel 718 deposited by laser powder bed fusion—Chances, use and challenges. *Addit. Manuf.* **2022**, *56*, 102888. [CrossRef]
7. Yang, Y.P.; Jamshidinia, M.; Boulware, P.; Kelly, S.M. Prediction of microstructure, residual stress, and deformation in laser powder bed fusion process. *Comput. Mech.* **2018**, *61*, 599–615. [CrossRef]
8. Wang, D.; Song, C.; Yang, Y.; Bai, Y. Investigation of crystal growth mechanism during selective laser melting and mechanical property characterization of 316L stainless steel parts. *Mater. Des.* **2016**, *100*, 291–299. [CrossRef]
9. Bugatti, M.; Semeraro, Q. Limitations of the inherent strain method in simulating powder bed fusion processes. *Addit. Manuf.* **2018**, *23*, 329–346. [CrossRef]
10. Gouge, M.; Denlinger, E.; Irwin, J.; Li, C.; Michaleris, P. Experimental validation of thermo-mechanical part-scale modeling for laser powder bed fusion processes. *Addit. Manuf.* **2019**, *29*, 100771. [CrossRef]
11. Gockel, J.; Sheridan, L.; Koerper, B.; Whip, B. The influence of additive manufacturing processing parameters on surface roughness and fatigue life. *Int. J. Fatigue* **2019**, *124*, 380–388. [CrossRef]

12. Stokes, R.M.; Yadollahi, A.; Priddy, M.W.; Bian, L.; Hammond, V.H.; Doude, H.R. Effects of Build Interruption and Restart Procedure on Microstructure and Mechanical Properties of Laser Powder Bed Fusion Al-Si-10Mg. *J. Mater. Eng. Perform.* **2022**, *32*, 1576–1588. [CrossRef]

13. Cherry, J.A.; Davies, H.M.; Mehmood, S.; Lavery, N.P.; Brown, S.G.R.; Sienz, J. Investigation into the effect of process parameters on microstructural and physical properties of 316L stainless steel parts by selective laser melting. *Int. J. Adv. Manuf. Technol.* **2015**, *76*, 869–879. [CrossRef]

14. Hodge, N.E.; Ferencz, R.M.; Solberg, J.M. Implementation of a thermomechanical model for the simulation of selective laser melting. *Comput. Mech.* **2014**, *54*, 33–51. [CrossRef]

15. Ganeriwala, R.K.; Strantza, M.; King, W.E.; Clausen, B.; Phan, T.Q.; Levine, L.E.; Brown, D.W.; Hodge, N.E. Evaluation of a thermomechanical model for prediction of residual stress during laser powder bed fusion of Ti-6Al-4V. *Addit. Manuf.* **2019**, *27*, 489–502. [CrossRef]

16. Lindgren, L.-E.; Lundbäck, A.; Fisk, M.; Pederson, R.; Andersson, J. Simulation of additive manufacturing using coupled constitutive and microstructure models. *Addit. Manuf.* **2016**, *12*, 144–158. [CrossRef]

17. Dantin, M.J.; Furr, W.M.; Priddy, M.W. Toward a Physical Basis for a Predictive Finite Element Thermal Model of the LENS™ Process Leveraging Dual-Wavelength Pyrometer Datasets. *Integrating Mater. Manuf. Innov.* **2022**, *11*, 407–417. [CrossRef]

18. Soundararajan, B.; Sofia, D.; Barletta, D.; Poletto, M. Review on modeling techniques for powder bed fusion processes based on physical principles. *Addit. Manuf.* **2021**, *47*, 102336. [CrossRef]

19. Baiges, J.; Chiumenti, M.; Moreira, C.A.; Cervera, M.; Codina, R. An adaptive Finite Element strategy for the numerical simulation of additive manufacturing processes. *Addit. Manuf.* **2021**, *37*, 101650. [CrossRef]

20. Hodge, N.E.; Ferencz, R.M.; Vignes, R.M. Experimental comparison of residual stresses for a thermomechanical model for the simulation of selective laser melting. *Addit. Manuf.* **2016**, *12*, 159–168. [CrossRef]

21. Denlinger, E.R.; Michaleris, P. Effect of stress relaxation on distortion in additive manufacturing process modeling. *Addit. Manuf.* **2016**, *12*, 51–59. [CrossRef]

22. Johnson, K.L.; Emery, J.M.; Hammetter, C.I.; Brown, J.A.; Grange, S.J.; Ford, K.R.; Bishop, J.E. Predicting the reliability of an additively-manufactured metal part for the third Sandia fracture challenge by accounting for random material defects. *Int. J. Fract.* **2019**, *218*, 231–243. [CrossRef]

23. Dantin, M.J.; Priddy, M.W. A Rate- and Temperature-Dependent Thermomechanical Internal State Variable Model of the Directed Energy Deposition Process. *J. Mater. Eng. Perform.* **2024**, *33*, 4051–4064. [CrossRef]

24. Marin, E.B.; Bammann, D.J.; Regueiro, R.A.; Johnson, G.C. *On the Formulation, Parameter Identification and Numerical Integration of the EMMI Model: Plasticity and sotropic Damage*; Sandia National Laboratories: Albuquerque, NM, USA, 2006.

25. Pant, P.; Proper, S.; Luzin, V.; Sjöström, S.; Simonsson, K.; Moverare, J.; Hosseini, S.; Pacheco, V.; Peng, R.L. Mapping of residual stresses in as-built Inconel 718 fabricated by laser powder bed fusion: A neutron diffraction study of build orientation influence on residual stresses. *Addit. Manuf.* **2020**, *36*, 101501. [CrossRef]

26. Hibbett, Karlsson and Sorensen. *ABAQUS/Standard: User's Manual*; Hibbitt, Karlsson and Sorenson Incorporated: Pawtucket, RI, USA, 1998; Volume 1.

27. Betts, J.L.; Downs, W.; Dantin, M.J.; Priddy, M.W. Examining the Gpu Acceleration Speed-Up for Finite Element Modeling of Additive Manufacturing. Available online: https://repositories.lib.utexas.edu/server/api/core/bitstreams/c004ad59-d8d5-4f4b-abf5-92eea1458740/content (accessed on 26 July 2024).

28. An, N.; Yang, G.; Yang, K.; Wang, J.; Li, M.; Zhou, J. Implementation of Abaqus user subroutines and plugin for thermal analysis of powder-bed electron-beam-melting additive manufacturing process. *Mater. Today Commun.* **2021**, *27*, 102307. [CrossRef]

29. Solid Edge Documentation. Siemens. Available online: https://docs.sw.siemens.com/en-US/documents/246738425/PL20190201104957790?start=0 (accessed on 26 July 2024).

30. Skroch, M. Coreform CubitTM 2024.7 User Documentation. Coreform. Available online: https://coreform.com/cubit_help/cubithelp.htm#t=cubit_users_manual.html (accessed on 26 July 2024).

31. Luo, Z.; Zhao, Y. A survey of finite element analysis of temperature and thermal stress fields in powder bed fusion Additive Manufacturing. *Addit. Manuf.* **2018**, *21*, 318–332. [CrossRef]

32. Song, X.; Feih, S.; Zhai, W.; Sun, C.-N.; Li, F.; Maiti, R.; Wei, J.; Yang, Y.; Oancea, V.; Romano Brandt, L.; et al. Advances in additive manufacturing process simulation: Residual stresses and distortion predictions in complex metallic components. *Mater. Des.* **2020**, *193*, 108779. [CrossRef]

33. Rahimi, S.; King, M.; Dumont, C. Stress relaxation behaviour in IN718 nickel based superalloy during ageing heat treatments. *Mater. Sci. Eng. A* **2017**, *708*, 563–573. [CrossRef]

34. Failla, D.P., Jr.; Nguyen, C.J. AMPES: Additive Manufacturing Process Event Series Generator. Available online: https://github.com/Computational-Mechanics-Materials-Lab/AMPES (accessed on 8 June 2024).

35. Goldak, J.; Chakravarti, A.; Bibby, M. A new finite element model for welding heat sources. *Metall. Trans. B* **1984**, *15*, 299–305. [CrossRef]

36. Kiran, A.; Li, Y.; Hodek, J.; Brázda, M.; Urbánek, M.; Džugan, J. Heat Source Modeling and Residual Stress Analysis for Metal Directed Energy Deposition Additive Manufacturing. *Materials* **2022**, *15*, 2545. [CrossRef]

37. Hodgson, G. Slic3r Manual. Available online: https://manual.slic3r.org/ (accessed on 10 May 2024).

38. Mohr, G.; Altenburg, S.J.; Hilgenberg, K. Effects of inter layer time and build height on resulting properties of 316L stainless steel processed by laser powder bed fusion. *Addit. Manuf.* **2020**, *32*, 101080. [CrossRef]

39. Bammann, D.J. An internal variable model of viscoplasticity. *Int. J. Eng. Sci.* **1984**, *22*, 1041–1053. [CrossRef]

40. Goldak, J.A.; Akhlagi, M. *Computational Welding Mechanics*; Springer: New York, NY, USA, 2005.

41. Marin, E.; Bammann, D.; Brown, A.; El Kadiri, H.; Costley, R.; Wang, P.; Horstemeyer, M. Modeling the Hot Forging of Nickel-Based Superalloys: IN718 and Alloy 718Plus®. In Proceedings of the 7th International Symposium on Superally 718 and Derivatives, Pittsburgh, PA, USA, 10–13 October 2010; pp. 331–342.

42. Lane, B.; Jacquemetton, L.; Piltch, M.; Beckett, D. *Thermal Calibration of Commercial Melt Pool Monitoring Sensors on a Laser Powder Bed Fusion System*; US Department of Commerce, National Institute of Standards and Technology: Gaithersburg, MD, USA, 2020; p. 20.

43. Ma, L.; Bin, H. Temperature and stress analysis and simulation in fractal scanning-based laser sintering. *Int. J. Adv. Manuf. Technol.* **2007**, *34*, 898–903. [CrossRef]

44. Phan, T.Q.; Strantza, M.; Hill, M.R.; Gnaupel-Herold, T.H.; Heigel, J.; D'Elia, C.R.; DeWald, A.T.; Clausen, B.; Pagan, D.C.; Peter Ko, J.Y.; et al. Elastic Residual Strain and Stress Measurements and Corresponding Part Deflections of 3D Additive Manufacturing Builds of IN625 AM-Bench Artifacts Using Neutron Diffraction, Synchrotron X-Ray Diffraction, and Contour Method. *Integrating Mater. Manuf. Innov.* **2019**, *8*, 318–334. [CrossRef]

45. Pant, P.; Salvemini, F.; Proper, S.; Luzin, V.; Simonsson, K.; Sjöström, S.; Hosseini, S.; Peng, R.L.; Moverare, J. A study of the influence of novel scan strategies on residual stress and microstructure of L-shaped LPBF IN718 samples. *Mater. Des.* **2022**, *214*, 110386. [CrossRef]

46. Dejene, N.D.; Lemu, H.G. Current Status and Challenges of Powder Bed Fusion-Based Metal Additive Manufacturing: Literature Review. *Metals* **2023**, *13*, 424. [CrossRef]

47. Guillen, D.; Wahlquist, S.; Ali, A. Critical Review of LPBF Metal Print Defects Detection: Roles of Selective Sensing Technology. *Appl. Sci.* **2024**, *14*, 6718. [CrossRef]

48. Denlinger, E.R.; Gouge, M.; Irwin, J.; Michaleris, P. Thermomechanical model development and in situ experimental validation of the Laser Powder-Bed Fusion process. *Addit. Manuf.* **2017**, *16*, 73–80. [CrossRef]

49. ASM Aerospace Specification Metals Inc. Special Metals INCONEL® Alloy 718. Available online: https://asm.matweb.com/search/SpecificMaterial.asp?bassnum=NINC34 (accessed on 22 July 2024).

50. Knapp, G.L.; Raghavan, N.; Plotkowski, A.; DebRoy, T. Experiments and simulations on solidification microstructure for Inconel 718 in powder bed fusion electron beam additive manufacturing. *Addit. Manuf.* **2019**, *25*, 511–521. [CrossRef]

51. Stainless Steel-Grade 316 (UNS S31600). AZO Materials. Available online: https://www.azom.com/properties.aspx?ArticleID=863 (accessed on 22 July 2024).

52. ASM Aerospace Specification Metals Inc. AISI Type 316L Stainless Steel, Annealed Bar. Available online: https://asm.matweb.com/search/SpecificMaterial.asp?bassnum=MQ316Q (accessed on 22 July 2024).